SUPPORTING INFORMATION

Tracing the *post-mortem* history of Egyptian mummies using nuclear microprobe analysis of trace metal elements and mineral dust particles

Didier Gourier*[a,b], Océane Anduze,[a,b] Quentin Lemasson,[b,c] Laurent Pichon,[b,c] Thomas Calligaro,[b,c] Agnès Lattuati-Derieux,[b,a] Laurent Binet,[a,b]

[a] PSL University, Chimie-ParisTech, CNRS, Institut de Recherche de Chimie-Paris (IRCP), F-75005 Paris, France

[b] Centre de Recherche et de Restauration des Musées de France (C2RMF), Palais du Louvre, F-75001 Paris, France

[c] PSL University, Lab BC, CNRS, UAR 3506, C2RMF, Palais du Louvre, F-75001 Paris, France

*didier.gourier@chimieparistech.psl.eu

S1 DESCRIPTION OF SAMPLES

S1.1 The mummy of the *Musée de Boulogne-sur-Mer*

In September-october 1837, the *Musée de Boulogne-sur-Mer* acquired a set comprising the outer coffin (lost in World War I) and the middle coffin belonging to a priest named Nehemsimontou who lived towards the end of the dynasty XXV and the beginning of the XXVI (Fig. S1a), and containing a mummy supposedly belonging to this priest (Fig.S2). This set (2 coffins + mummy) had previously belonged to a Parisian collector, Dr. Antoine Hebray, whom his father had acquired probably around 1819 (Yoyotte, 1981). The inner coffin of this set is preserved in the *Musée de Grenoble* (Fig.S1b). Comparison of the dimensions of the inner coffin and the mummy led to believe that the latter is unlikely to be Nehemsimontou.

A handwritten label on the inner coffin reads (Fig.S1b): "*momie des catacombes de Thèbes (…) rapportée par Vivant Denon de l'expédition d'Egypte, 1799* ». However, Jean Yoyotte has convincingly shown that Vivant Denon never owned this mummy (Yoyotte, 1981).

Figure S1: a) Intermediate coffin of Nehemsimontou, which contained the mummy when it was acquired by the city of Boulogne-sur-Mer in 1837, on display for the '*Serving the Gods of Egypt'* exhibition in Grenoble, France (25/10/2018 to 27/01/2019), *Château-Musée de Boulogne-sur-Mer* © Milky - CC-BY-SA ; b) Upper part of the internal coffin in which the mummy of Nehemsimontou was originally placed; c) Photograph of a detail of the internal coffin showing the inscription indicating that the coffin was brought back by Vivant-Denon (adapted from Dewachter, 1979); End of Dynasty XXV - beginning of Dynasty XXVI, *Musée de Grenoble* (MG 1995) © J. Cordier (lavieb-aile) .

The samples analyzed are fragments that broke away from the mummy's head and neck during its consolidation at C2RMF in 2004 (Dal-Prà, 2004). Figure S2 shows the mummy's head and neck, with three components making up the samples analyzed in this work: 1) a portion of the linen cloth strips stuck to the skull cap (sample 2, and possibly sample 1), a dark dull brown material covering the skin of the head and neck, and a fragments of shiny black material (sample 3) on the mummy's neck (Fig. S2) and hips covering the dull brown matter (Dal-Prà, 2004).

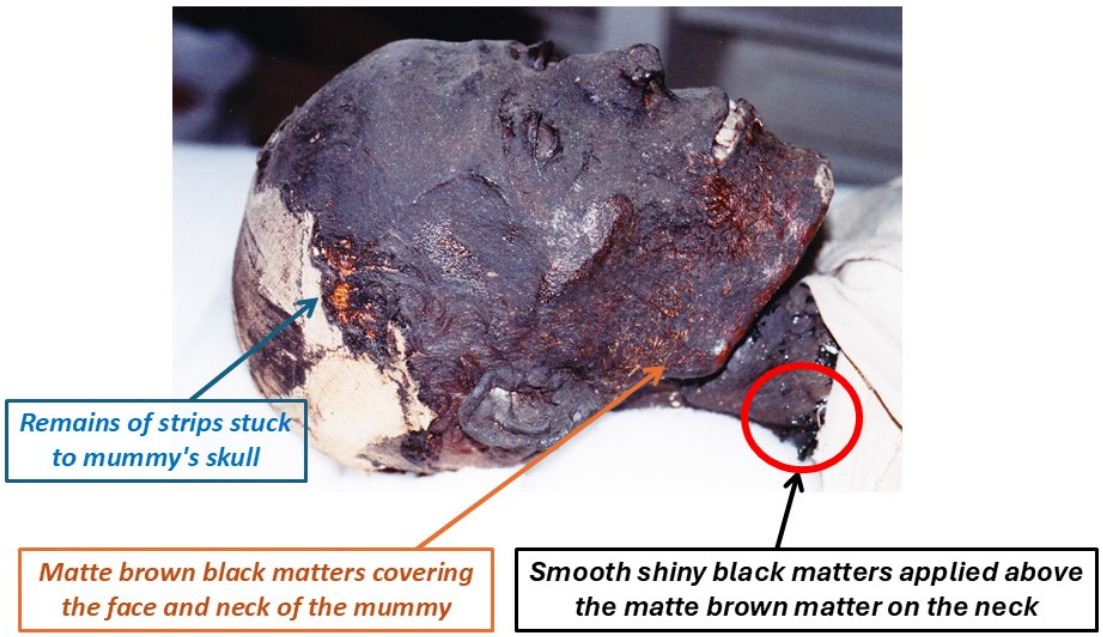

Figure S2: Photograph of the head and neck of the mummy from the *Château-Musée de Boulogne-sur-Mer*. Note the presence of two types of black material, applied one on top of the other. Photograph taken from the mummy restoration report (Dal-Prà 2004) @ Dal-Prà.

S1.2 The other studied mummies

Another series of samples of embalming matter taken from 14 mummies were also analyzed by coupled PIXE-IBIL mapping for comparison with the BSM mummy. These samples are described in details in Anduze *et al*. 2025. They belong to 9 birds (numbered 1 to 14), two rams (An1, An2/An3), one crocodile (An4), one human mummy (Hum2) and a fragment of black matter taken from the bottom of a human coffin (Hum1).

Sample	Museum	Reference	Mummy	Period	Site
1	Confluences, Lyon	90002515	Bird of prey	ind	Kom Ombo
3	Confluences, Lyon	90002517	Bird of prey	Roman	Giza
4	Confluences, Lyon	90002518	Bird of prey	Roman	Giza
6	Confluences, Lyon	90010018	Ibis	3rd Int. period	Saqqarah
8	Confluences, Lyon	90002801	Bird of prey	Roman	Giza
10	Confluences, Lyon	90010028	Ibis	ind	Kom Ombo
11	Confluences, Lyon	90010022	Ibis	Late period	Roda
12	Confluences, Lyon	90010027	Ibis	Late to Ptolem.	Roda
14	Confluences, Lyon	90010066	Bird of prey	Ptolemaic	Roda
An1	Louvre, Paris	INV 12667	Ram	Ptolem./Roman	Elephantine
An2/An3	Thomas Dobrée, Nantes	D 961.2.140/ INV 1384	Ram	Roman	Elephantine
An4	Confluences, Lyon	90001840	Crocodile	Ptolemaic	Upper Egypt
Hum1	Archevêques, Narbonne	N.P.4140, 841.4.1.1	Human coffin	Ptolemaic	Upper Egypt (Abydos ?)
Hum2	Hiéron, Paray	FZ30827	Human	Late Period	Upper Egypt (Akhmin ?)

Table S1: Other mummies from French museums; the bird mummies and the crocodile mummy An4 come from the collection of the *Musée des Confluences*, Lyon; the ram An1 comes from the Louvre Museum; rams An2/An3 come from the *Musée Thomas Dobrée* Museum, Nantes; the coffin Hum1 comes from the *Palais-musée des Archevêques*, Narbonne, France; the human mummy Hum2 comes from the *Musée Hieron*, Paray-le-Monial, France.

S2 THE EXTERNAL PROTON BEAM ANALYSIS SYSTEM

S2.1 The nuclear microprobe detection system

The configuration of the detection system installed on AGLAE is shown in figure S3. In addition to the viewing camera and the dose detector, it comprises: 1) three high-energy PIXE detectors (HE), covered with a 100 mm-thick Mylar filter, and one unfiltered low-energy PIXE detector (LE), positioned at 45° (LE) and 50° (HE) to the beam axis, respectively; 2) a PIPS detector at 130° to the beam axis for detection of backscattered protons (EBS); 3) an optical fiber to detect the optical emission (IBIL); 4) an HPGE detector to detect the γ-photons originating from nuclear reactions (PIGE).

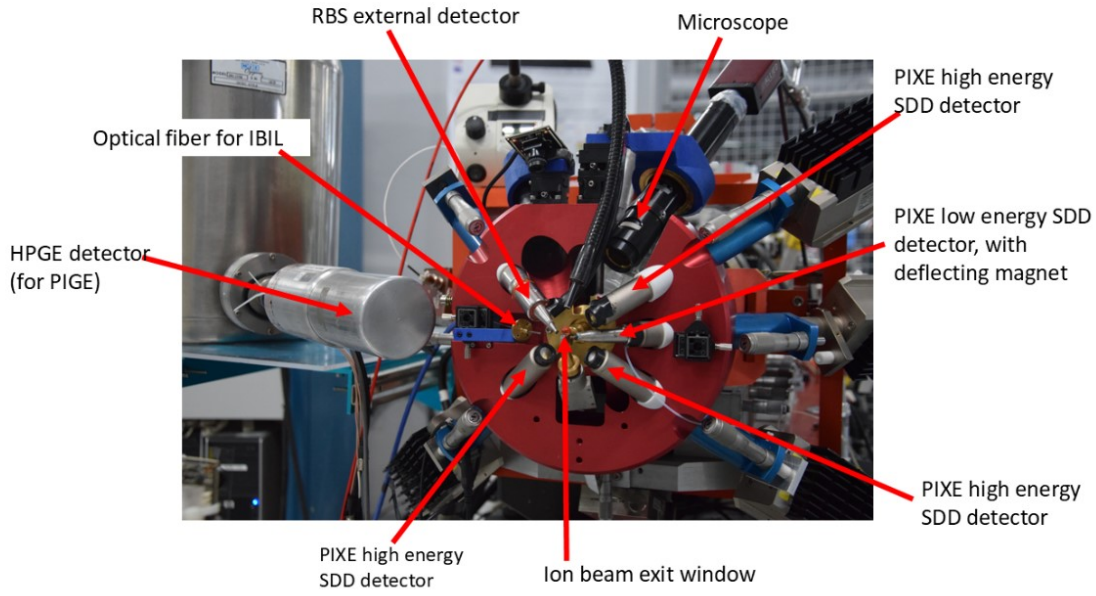

Figure S3: Schematic diagram of the AGLAE multidetector; the proton beam direction is perpendicular to the image; @ C2RMF/B.Moignard.

S2.2 PIXE and IBIL mapping

Samples		Number of pixels	Selected pixels	Collected beam charge (μC)	Beam intensity (nA)	Beam fluence (μC.cm^{-2})
Dead Sea bitumen (DS)	DS(1)	10 000	9931	14	4.2	223.0
	DS(2)	1600	1581	1.1	1.0	111.4
Corpus A (birds)	*1*	1600	912	1.1	0.9	111.3
	3	1600	1338	1.1	0.9	111.3
	4	1560	1314	1.1	0.9	114.2
	6	1600	1437	1.1	1.3	111.4
	8	1600	1419	1.1	1.3	111.4
	10	1600	1130	1.1	0.9	111.4
	11	1600	1131	1.1	1.0	111.3
	12	1600	1285	1.1	1.2	111.4
	14	1600	1494	1.1	0.9	111.4
Corpus B animals (An1-5); human (Hum1-2)	*An1*	6400	3712	8.9	6.6	223.0
	An2(1)	1600	852	1.1	1.1	111.3
	An2(2)	1600	1124	1.1	nd	111.4
	An3	12 000	11 062	16.7	6.5	223.0
	An5	6400	4596	8.9	6.5	223.0
	Hum1	9600	9189	13.4	6.7	223.1
	Hum2(1)	14 000	11 782	19.5	6.7	223.0
	Hum2(2)	6400	6400	4.5	6.8	111.6
BSM mummy	$1\alpha_1$	14 400	11 334	20.1	5.7	223.0
	$1\alpha_2$	1600	1224	2.2	6.4	223.0
	$1\beta_3$	10 000	7564	13.9	6.5	223.1
	$1\beta_4$	10 000	6070	13.9	6.6	223.1
	$1\beta_5$	3600	2805	5.0	6.6	223.1
	$1\beta_6$	10 000	7892	13.9	6.6	223.1
	$2\beta_1$	1600	603	1.1	1.0	111.3
	$2\beta_2$	1600	780	1.1	0.9	108.0
	$2\beta_3$	1600	587	1.1	0.9	111.4
	$2\alpha_4$	400	293	1.1	1.0	445.2
	$3\alpha_1$	11 200	9546	15.6	6.7	223.0
	$3\alpha_2$	2400	1784	3.4	6.7	223.2
	$3\alpha_3$	9600	8650	13.4	6.9	223.1

Table S2: Experimental conditions for PIXE mappings of homogeneous zones.

Table S2 shows the experimental conditions used for the PIXE, IBIL, and EBS mappings. We have also considered the absorbed dose D, which is directly related to the beam fluence φ and the reduced stopping power S/ρ of the incident particles (protons in this case) in the analyzed material.

$D = 10^6\ [\varphi] \bullet [S/\rho]$,

with D in Gy, φ in μC/cm², and S/ρ in MeV/(mg/cm²). One of the authors (TC) has developed a Python code to calculate the exposure dose D in real time during analysis, with two key values, at the surface

of the sample and at the Bragg peak near the end of the ion path. This program uses the fundamental SRIM data that are also used in the GUPIX code.

According to Table S2, here are the values of D for the three fluences φ of 3 MeV protons mostly used in the study and the assumption of a bitumen composition of $C_{84}O_{13}S_3$ (Bragg peak at 127 μm).

φ in μC/cm²	D at the surface, in Gy	D at the Bragg peak (80 keV)
222	22.9×10^6	157×10^6
445	45.7×10^6	316×10^6
111	11.4×10^6	79×10^6

It can be seen that D reaches very high values due to the light matrix and very high fluence (required by EBS). In general, changes are observed in brittle materials starting at 100,000 Gy. However, we did not observe any visual changes in the samples, even when the surface analyzed was the strip covering the mummy.

AGLAEMap is a software package developed by the AGLAE team, which simultaneously displays and analyzes all families of data collected during a single run (HE/LE PIXE, EBS and IBIL in our case). For each detector, the mapping and total spectrum (sum of all mappings / all spectra per element) are displayed by default. A wavelength/energy range on the IBIL/PIXE spectrum to instantaneously display the mapping corresponding to that range. When a region of interest (ROI) is selected, these changes are reflected in real time in the spectra and mappings of all data sets. To compare the PIXE and IBIL mappings qualitatively, the entire IBIL spectrum is first scanned to identify any luminescence spots. Converting the IBIL spectrum with the *MPS* (Maximum Pixel Spectrum) algorithm, which selects the pixels corresponding to the maximum intensity for each channel in the mapping (Alfeld and Janssens, 2015), proved very useful for highlighting low-intensity luminescence emissions that did not stand out on the raw spectrum. *AGLAEmap* can be used to compare PIXE and IBIL mappings, which enabled an initial qualitative comparison of these datasets in order to identify spatial correlations between luminescent spots in IBIL and micro-dusts detected by PIXE. The luminescent spots identified on the IBIL mappings were labelled according to their location in the map, by transferring the dimensions of this map to those of a square according to a grid system (Fig.S4b).

The complete IBIL analysis of given sample is carried out in five main steps using *AGLAEMap* software: 1) selection of a mapped area; 2) wavelength scanning of the total IBIL spectrum to locate any luminescent spots; 3) selection of each luminescent spot, named after its location in the mapping; 4) extraction of the luminescence spectrum of each spot of interest; 4)

Apply the IBIL spot selection to the PIXE mapping to extract the PIXE spectra corresponding to the spatial area of the spot. By injecting these spectra into the *GUPIX* software, it is possible to quantify the elements at the level of a luminescent spot, and thus couple these two pieces of information.

Figure S4a shows an example of identification of mineral microparticles from a single IBIL spectrum on the surface of a feather of an ibis mummy (sample 11 of corpus A). Each component of the spectrum corresponds to specific luminescent species (Fe^{III}, Mn^{II}, Cu^{II}, intrinsic point defects) and specific luminescent spots. Except in the case of calcite, where identification was based solely on the luminescence of Mn^{II} impurities (Ca is identifiable by PIXE, but it is abundant throughout the samples), the other minerals were identified by coupling IBIL and PIXE. For example, feldspars (albite) were identified by the luminescence of Fe^{III} impurities and by the Al/Si ratios of the light spots measured by PIXE, and cuprorivaite was identified by the luminescence of Cu^{II} around 900 nm and by Cu K lines at 8.04 keV and 8.91 keV (see Fig.7 of the main article).

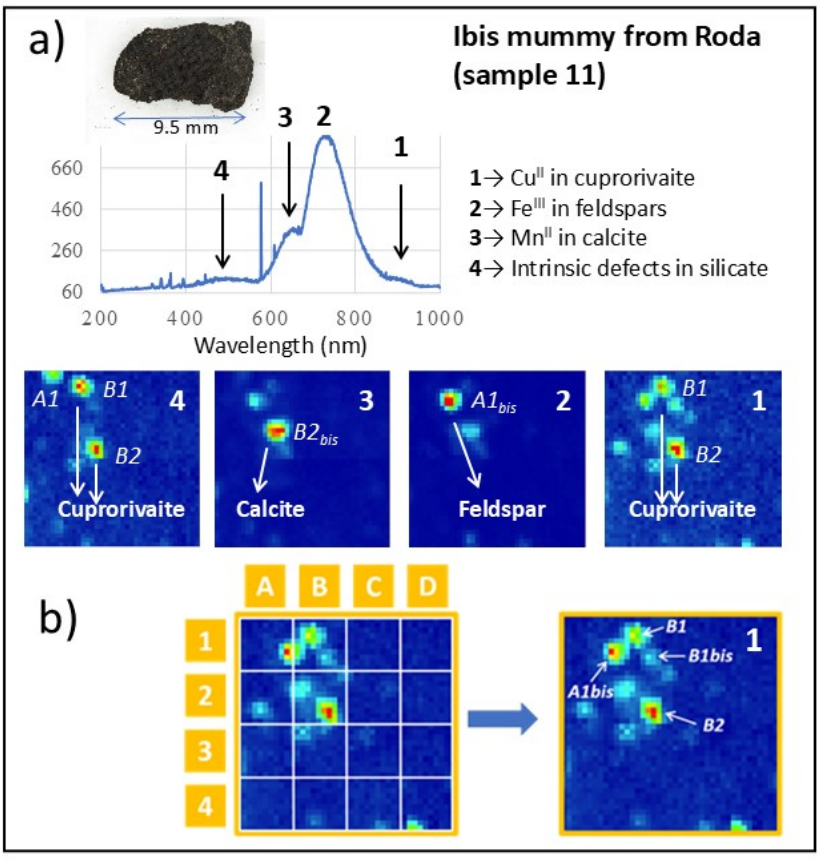

Figure S4: a) IBIL spectrum of a feather fragment from an ibis mummy (sample 11), with IBIL mappings (1000×1000 µm²) of four selected wavelength ranges (labelled 1 to 4) corresponding to four luminescent peaks; three types of mineral microparticles could be identified by their luminescence: Cuprorivaite (Cu^{II} and intrinsic defects), feldspar (Fe^{III} impurities), and calcite (Mn^{II} impurities); b) Labelling of microparticles according to a nomenclature grid, applied to the luminescence at 900 nm (cuprorivaite).

S2.3 Quantification of major and trace elements

The complex and crowded PIXE spectra were processed and interpreted step by step using *GUPIX* and *PyMca* software. *GUPIX* was designed for PIXE data analysis, and gives a better deconvolution than *PyMca*, since the *GUPIX* algorithm takes more rigorous account of the physical phenomena and their impact on the spectrum and its interpretation. However, *GUPIX* does not allow the extraction of corrected PIXE mappings after spectral deconvolution; indeed, the raw mappings directly obtained on *AGLAEmap* need to be re-extracted after spectrum processing, precisely to take into account phenomena, such as line overlap due to the limited resolution of the detector. This is enabled by *PyMca* via its "ROI Imaging Tool" (Pichon et al. 2015). This tool also makes it possible to obtain, for each identified element, the total mapping (K, L and M lines) but also the mappings for each individual K_α, K_β ... line. For each run, dozens of round-trips were sometimes made between the two software packages to interpret the PIXE spectra as completely as possible. The file containing the corrected PIXE mapping data obtained via *PyMca* was systematically exported to *DataImaging* software, which saves the mappings for each element and line, in linear and logarithmic scales. After screening all these mappings, only those of interest were finally re-extracted with *PyMca*, which enables them to be obtained at a slightly higher resolution. The final steps allow us to quantify the chemical elements present in the samples. While light (major) elements are present in the matrix and detected using the BE detector under helium flow, heavy elements are present in trace amounts in the material and are detected using the HE detectors. It would be possible to quantify only these two types of elements in *GUPIX*, but the software can only take one spectrum into account at a time, and this processing would be extremely slow. The *TRAUPIXE* software allows us to rapidly obtain elemental quantifications for hundreds of BE/HE pairs of PIXE spectra, based on spectra of standards of known composition analyzed at the same time as our samples. Elemental quantification of a sample by *GUPIX* normally requires knowledge of the material's matrix composition. However, this matrix is not known *a priori* for our complex materials, and moreover it is mainly made up of light elements (C, O, N, H) which are not detected by PIXE, and of heavier elements of trapped mineral dust. In the case of a mineral matrix, *GUPIX* quantifies the elements required, and then normalizes the sum of relative contents to 100%. But this is only correct if all major elements are measured by PIXE. In the case of biological/organic matter, we indicated to the software that the sum of the relative contents measured would be less than 100%, by declaring the presence of two elements (C and

O) not detected by PIXE. As *GUPIX* cannot therefore base its elemental quantification on the composition of a known matrix, each run was associated with the BE spectrum of a standard of perfectly known chemical composition. The standard used was a sample of diorite (DrN), one of the geochemical reference materials certified by SARM (*Service d'Analyse des Roches et des Minéraux*), whose major and trace element composition are precisely known. This standard was systematically recorded two times each day of data acquisition on AGLAE, before and after analyzing the mummy samples. Calibration and parameterization of the standard spectra was carried out on *GUPIX*. The repeatability of DrN's morning and evening PIXE spectra was systematically checked by viewing them on the *PLotAndROI* software (developed by the AGLAE team). In addition, based on the precise composition known from the DrN standard, the parameter values, which are then reused by the software for the elemental quantification of our samples, were adjusted so as to obtain contents of several elements (CO_2, SiO_2, Fe_2O_3, Na_2O, CaO and V) as close as possible to the certified contents measured by SARM; the presence of water was also taken into account in relation to the theoretical values indicated by SARM. On the basis of these parameters, *GUPIX* calculated the major element contents in our samples without knowing the composition of the matrix. *TRAUPIXE* enables trace elements to be quantified using the pivot element method (Pichon et al. 2010). This element must be present in sufficient quantity to be detected by both the BE and HE detectors in the 3 - 10 keV range, for example calcium, iron or lead (Pichon et al. 2015). For highly complex composite materials such as our samples, whose composition is inherently difficult to analyze, determining two pivotal elements enabled us to perform a more rigorous quantification calculation. In the present work, Ca and Fe were chosen as pivotal elements. On a case-by-case basis, for each trace element of each run, the software automatically chose the most appropriate pivot.

The quantification of light elements is particularly affected by matrix effects, primarily by the strong absorption of low-energy X-rays (a few keV) within the target. The loss of proton energy as they penetrate the material has less influence on the quantification of light elements. In fact, due to the strong absorption of X-rays, only the PIXE emission from the near surface of the target is recovered, where the energy is practically constant. This effect notably impacts the PIXE dosage of light elements, primarily Al and Si, and was simulated with the GUPIX companion program GUYLS, which can simulate PIXE in stratified targets. It can be seen that Al and Si concentrations appear very weakened after around ten microns (Table S3).

Depth d (µm)	0	3.5	14	28	35	53.2
Ratio Ca/Al	1.00	1.35	3.27	9.94	27.79	71.11
Ratio Si/Al	1.00	1.15	1.71	2.86	4.61	7.21
Ratio Ca/Fe	1.00	0.92	0.92	0.83	0.77	0.72

Table S3: Effect of mineral particle trapping depth on light element quantification in the case of particles with theoretical element content Ca/Al =1, Si/Al = 1 and Ca/Fe = 1.

S3 PIXE ANALYSIS

S3.1 PIXE spectra

Experimental and simulated PIXE spectra of the homogeneous zones of the Boulogne-sur-Mer mummy samples are shown in Figure S5. The PIXE spectra of the other mummies (corpus A and B) are given in Anduze et al. 2025.

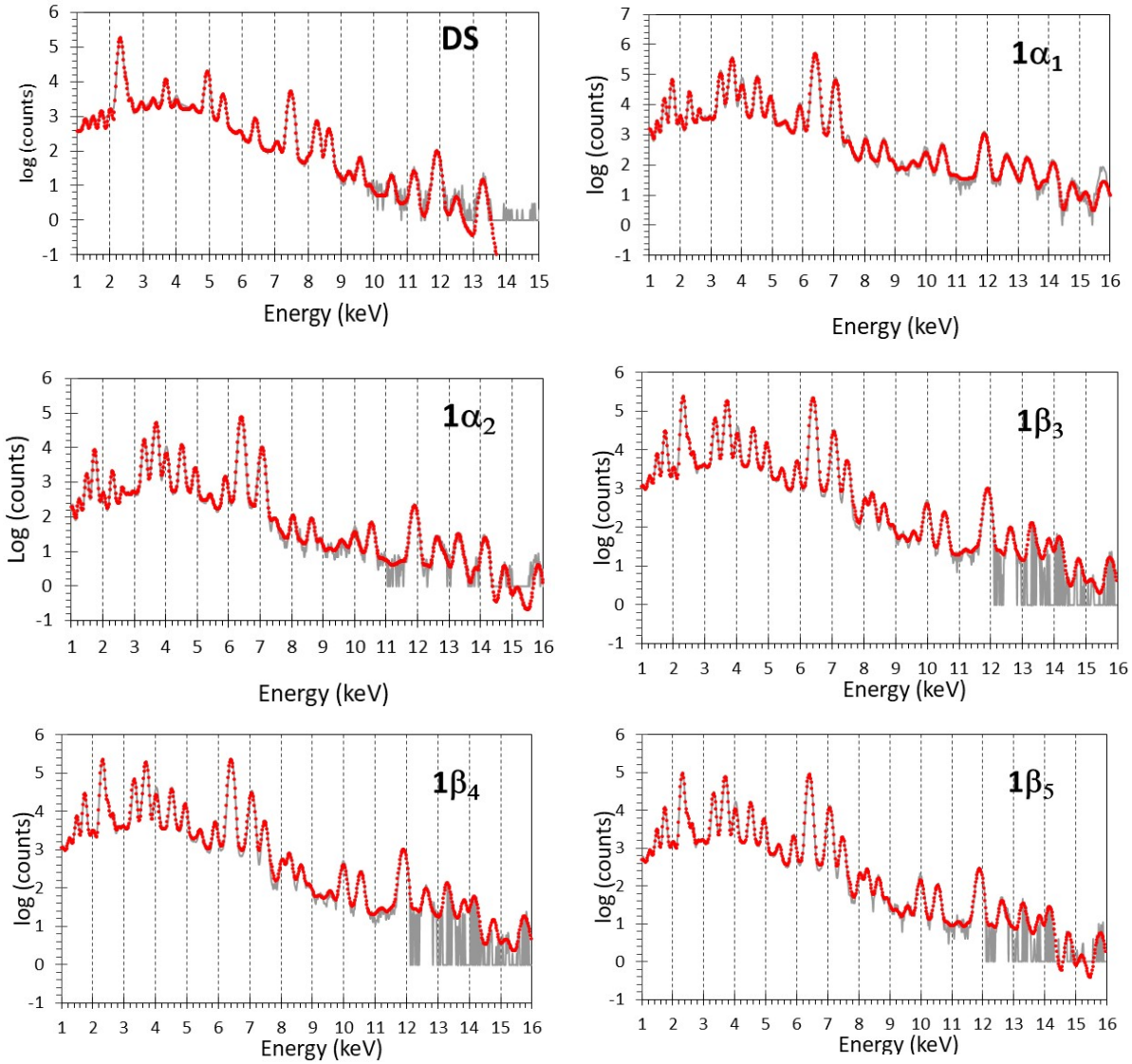

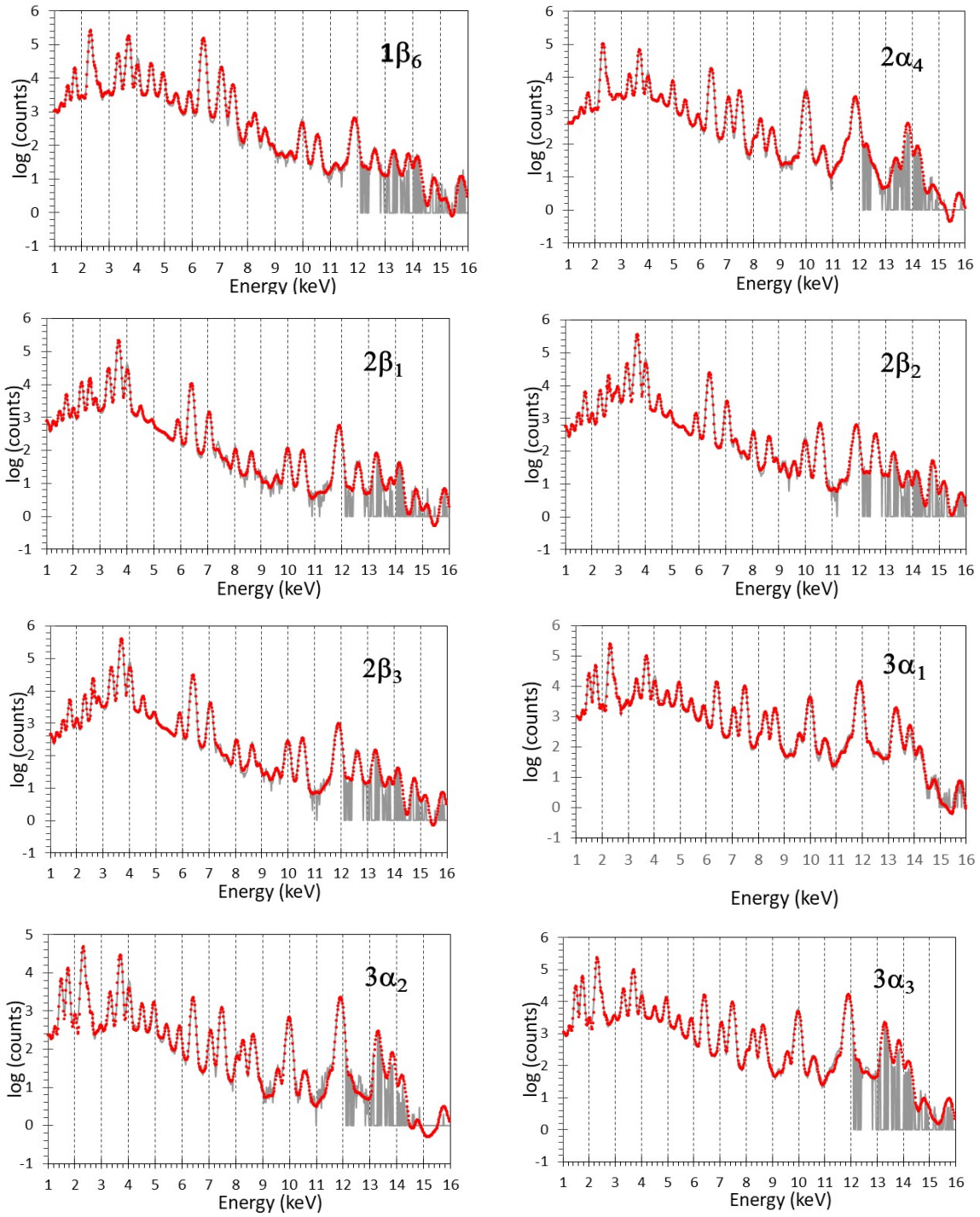

Figure S5: Experimental and simulated spectra of Dead Sea bitumen (DS) and of homogeneous zones of samples of the Boulogne-sur-Mer mummy.

S3.2 Markers of bitumen: V, Ni and S

	Concentrations (µg.g^{-1})		(weight %)
Mapping	**V**	**Ni**	**S**
DS(1)	888 ± 31	215 ± 12	7.4 ± 0.1
DS(2)	953 ± 31	318 ± 17	11.3 ± 0.04
$1\alpha_1$	(17 ± 2)	9 ± 0,4	0,6 ± 0,00
$1\alpha_2$	(31 ± 6)	19 ± 2	0,5 ± 0,00
$1\beta_3$	344 ± 9	293 ± 5	10,9 ± 0,05
$1\beta_4$	349 ± 10	315 ± 5	11,1 ± 0,1
$1\beta_5$	191 ± 7	240 ± 5	8.2 ± 0.05
$1\beta_6$	380 ± 8	323 ± 5	12,2 ± 0,1
$2\beta_1$	<3	(2 ± 1)	0,5 ± 0,01
$2\beta_2$	(2 ± 1)	(4 ± 1)	0,5 ± 0,01
$2\beta_3$	<2	(2 ± 1)	0,4 ± 0,01
$2\alpha_4$	266 ± 6	224 ± 5	7 ,1 ± 0,04
$3\alpha_1$	179 ± 3	158 ± 3	4.7 ± 0.0
$3\alpha_2$	288 ± 10	376 ± 11	9.6 ± 0.1
$3\alpha_3$	161 ± 3	143 ± 2	4.8 ± 0.04

Table S4: Vanadium, nickel and sulfur contents measured on homogeneous appearing PIXE mappings (without IBIL or PIXE spots) from the BSM mummy and Dead Sea bitumen samples; values in brackets are affected by an error greater than 25%, but the presence of these elements is assured by simulation of the PIXE spectra; in two cases the values have not been measured because they are below the LOD.

S3.3 Markers of mineral dust microparticles

		Concentration (µg.g^{-1})				
		Ti	**Cr**	**Mn**	**Fe**	**Cu**
Dead Sea bitumen (DS)	DS(1)	23 ± 2	21 ± 2	(2 ± 0.5)	21 ± 5	2 ± 0.5
	DS(2)	24 ± 5	26 ± 6	(1 ± 1)	34 ± 7	(3 ± 1)
Corpus A (birds)	*1*	129 ± 3	5 ± 1	29 ± 1	970 ± 29	6 ± 1
	3	77 ± 3	5 ± 1	11 ± 1	584 ± 19	29 ± 1
	4	1389±22	15 ± 1	125 ± 3	6742 ± 73	12 ± 1
	6	29 ± 3	(4 ± 1)	16 ± 1	743 ± 26	18 ± 1
	8	59 ± 2	5 ± 1	11 ± 1	477 ± 17	55 ± 2
	10	224 ± 6	4 ± 1	31 ± 1	1695 ± 34	7 ± 0.5
	11	851 ± 14	12 ± 3	340 ± 5	4875 ± 83	119 ± 2
	12	829 ± 14	9 ± 1	63 ± 2	3032 ± 49	10 ± 1
	14	56 ± 2	4 ± 1	10 ± 1	420 ± 18	59 ± 2
Corpus B rams (An1-3); crocodile (An5); human (Hum1-2)	*An1*	148 ± 4	10 ± 1	46 ± 1	1475 ± 19	68 ± 2
	An2(1)	65 ± 3	8 ± 1	24 ± 1	1024 ± 30	76 ± 3
	An2(2)	25 ± 2	(1 ± 0.5)	24 ± 1	210 ± 11	27 ± 2
	An3	104 ± 3	7 ± 2	30 ± 1	488 ± 6	103 ± 2
	An5	27 ± 2	6 ± 1	7 ± 1	231 ± 8	63 ± 2
	Hum1	8 ± 1	(2 ± 1)	9 ± 0.5	120 ± 3	19 ± 1
	Hum2(1)	8 ± 1	2 ± 1	4 ± 0.5	93 ± 2	19 ± 1
	Hum2(2)	(5 ± 1)	(3 ± 1)	3 ± 0.5	77 ± 3	17 ± 1
BSM mummy	$1\alpha_1$	951 ± 10	12 ± 1	96 ± 1	5042 ± 48	14 ± 1
	$1\alpha_2$	1281±25	24 ± 2	177 ± 5	10762 ± 187	31 ± 2
	$1\beta_3$	1808±24	46 ± 3	191 ± 4	8116 ± 75	31 ± 1
	$1\beta_4$	1893±27	42 ± 3	213 ± 4	9070 ± 107	35 ± 1
	$1\beta_5$	1070±18	29 ± 3	167 ± 4	7170 ± 90	38 ± 2
	$1\beta_6$	1216±19	44 ± 3	130 ± 3	5990 ± 78	14 ± 1
	$2\beta_1$	49 ± 3	(2 ± 1)	36 ± 2	481 ± 10	11 ± 1
	$2\beta_2$	70 ± 2	6 ± 1	44 ± 1	673 ± 8	26 ± 1
	$2\beta_3$	58 ± 2	(2 ± 1)	37 ± 1	584 ± 9	12 ± 1
	$2\alpha_4$	70 ± 3	18 ± 2	18 ± 1	739 ± 14	8 ± 1
	$3\alpha_1$	54 ± 2	13 ± 1	22 ± 1	173 ± 3	3 ± 0.3
	$3\alpha_2$	126 ± 8	(25 ± 4)	80 ± 4	457 ± 12	11 ± 2
	$3\alpha_3$	63 ± 2	11 ± 1)	29 ± 1	194 ± 3	4 ± 0.3

Table S5: Concentrations of several transition metal elements, measured in nearly homogeneous areas selected from PIXE mappings from the BSM mummy and corpus A and B mummies, as well as on Dead Sea bitumen (DS). Values in brackets have an error greater than 25%.

Samples		Concentrations (μg.g^{-1})			
		Al	Si	Mg	Ca
Bitumen (DS)	DS(1)	(95 ± 17)	160 ± 13	193 ± 28	605 ± 28
	DS(2)	(209 ± 33)	355 ± 25	494 ± 54	795 ± 325
Corpus A (birds)	*1*	689 ± 47	3375 ± 63	485 ± 60	5807 ± 58
	3	369 ± 35	1139 ± 35	(229 ± 45)	1173 ± 22
	4	7118 ± 108	23980 ± 94	2058 ± 78	7003 ± 77
	6	1354 ± 93	2696 ± 506	12772 ± 220	19767 ± 170
	8	472 ± 36	1392 ± 36	(176 ± 44)	1511 ± 25
	10	791 ± 40	2208 ± 44	224 ± 46	998 ± 22
	11	3417 ± 96	13064 ± 166	3783 ± 123	83285 ± 625
	12	9528 ± 131	29771 ± 223	1869 ± 83	9146 ± 102
	14	637 ± 38	1686 ± 46	(259 ± 44)	1117 ± 30
Corpus B rams (An1-3); crocodile (An5); human (Hum1-2)	*An1*	3076 ± 74	6810 ± 82	1510 ± 74	10271 ± 74
	An2(1)	3739 ± 83	10950 ± 115	115 ± 69	6687 ± 68
	An2(2)	385 ± 31	1261 ± 33	693 ± 43	1969 ± 27
	An3	1094 ± 29	2488 ± 32	1098 ± 40	7976 ± 65
	An5	227 ± 32	709 ± 30	(131 ± 45)	828 ± 25
	Hum1	(62 ± 19)	(73 ± 13)	(84 ± 30)	2137 ± 25
	Hum2(1)	(83 ± 18)	140 ± 12	229 ± 28	921 ± 14
	Hum2(2)	(42 ± 29)	(94 ± 20)	(128 ± 42)	511 ± 15
BSM mummy	*1*α_1	3863 ± 43	13405 ± 80	1009 ± 26	5728 ± 40
	1α_2	6979 ± 168	24805 ± 231	1660 ± 120	6508 ± 13
	1β_3	4220 ± 76	12519 ± 104	1080 ± 62	7472 ± 140
	1β_4	4694 ± 92	14054 ± 150	1235 ± 76	16788 ± 180
	1β_5	4395 ± 106	12377 ± 140	1276 ± 96	9956 ± 105
	1β_6	3047 ± 64	8361 ± 94	736 ± 59	14302 ± 156
	2β_1	883 ± 57	2154 ± 60	718 ± 73	9264 ± 90
	2β_2	1523 ± 66	4993 ± 83	1273 ± 81	9806 ± 89
	2β_3	901 ± 59	3182 ± 71	600 ± 73	7280 ± 84
	2α_4	870 ± 48	2536 ± 51	(306 ± 60)	3283 ± 54
	3α_1	5299 ± 63	8807 ± 96	157 ± 15	2666 ± 5
	3α_2	16885 ± 260	28935 ± 341	636 ± 90	4902 ± 92
	3α_3	6121 ± 70	11280 ± 115	193 ± 15	2667 ± 34

Table S6: Aluminum, silicon and sulfur contents measured on the homogeneous zones of samples from the Boulogne-sur-Mer mummy and corpus A and B mummies, as well as on Dead Sea bitumen (DS). Values in brackets have an error of over 25%, but the presence of these elements is assured.

Luminescent particles	Concentrations (weight %)		
	Al	Si	S
$1\alpha_1$ _A1-B2	0,43 ± 0,03	1,34 ± 0,03	0,16 ± 0,01
$1\alpha_1$ _A2	0,71 ± 0,04	1,89 ± 0,05	0,24 ± 0,01
$1\alpha_1$ _A2bis	0,36 ± 0,03	1,39 ± 0,04	0,36 ± 0,02
$1\alpha_1$ _A3	0,78 ± 0,04	3,00 ± 0,06	0,31 ± 0,02
$1\alpha_1$ _A3-A4	1,01 ± 0,06	2,92 ± 0,07	0,58 ± 0,03
$1\alpha_1$ _A3bis	0,48 ± 0,04	1,48 ± 0,06	0,20 ± 0,02
$1\alpha_1$ _A4	0,70 ± 0,03	2,12 ± 0,04	0,41 ± 0,02
$1\alpha_1$ _A4bis	0,70 ± 0,04	1,92 ± 0,04	0,39 ± 0,02
$1\alpha_1$ _B1	1,02 ± 0,06	2,84 ± 0,08	0,22 ± 0,02
$1\alpha_1$ _B1bis	0,93 ± 0,05	2,63 ± 0,06	0,23 ± 0,01
$1\alpha_1$ _B3-B4	0,37 ± 0,02	0,97 ± 0,03	0,23 ± 0,01
$1\alpha_1$ _B4	0,75 ± 0,05	1,92 ± 0,06	0,36 ± 0,02
$1\alpha_1$ _B4bis	0,69 ± 0,04	1,84 ± 0,04	0,39 ± 0,02
$1\alpha_1$ _C3-C4	1,10 ± 0,05	3,79 ± 0,06	0,27 ± 0,01
$1\alpha_1$ _C4	0,70 ± 0,04	2,29 ± 0,07	0,20 ± 0,02
$1\alpha_2$ _B1-B2	0,68 ± 0,05	2,19 ± 0,06	0,36 ± 0,02
$1\alpha_2$ _B3-B4	0,75 ± 0,05	1,90 ± 0,05	0,26 ± 0,02
$1\alpha_2$ _C1-D2	0,37 ± 0,03	1,31 ± 0,05	0,18 ± 0,01
$1\beta_3$ _B2-B3	0,77 ± 0,04	2,53 ± 0,05	1,52 ± 0,03
$1\beta_4$ _A2	0,24 ± 0,03	0,72 ± 0,03	1,94 ± 0,04
$1\beta_4$ _B2	1,03 ± 0,03	3,98 ± 0,05	1,72 ± 0,02
$1\beta_4$ _C2	0,36 ± 0,03	1,12 ± 0,03	3,87 ± 0,05
$1\beta_5$ _A1	0,80 ± 0,03	2,83 ± 0,04	3,86 ± 0,05
$1\beta_6$ _A4	0,54 ± 0,02	1,88 ± 0,03	4,16 ± 0,04
$1\beta_6$ _B4	0,43 ± 0,03	1,11 ± 0,03	5,74 ± 0,06
$1\beta_6$ _C2	0,25 ± 0,02	0,98 ± 0,03	6,21 ± 0,07
$2\beta_1$_A1-A2	(0,09 ± 0,04)	0,21 ± 0,04	0,55 ± 0,04
$2\beta_1$_A2-A3	2,18 ± 0,22	2,95 ± 0,19	0,55 ± 0,07
$2\beta_2$_B3	1,26 ± 0,19	1,85 ± 0,23	0,31 ± 0,06
$2\beta_2$_C4-D4	0,39 ± 0,07	0,94 ± 0,08	0,37 ± 0,05
$2\beta_2$_D3bis	(0,16 ± 0,06)	0,22 ± 0,04	0,64 ± 0,05
$2\beta_3$_A4	0,18 ± 0,04	1,13 ± 0,07	0,20 ± 0,03
$2\beta_3$_C1	(0,16 ± 0,05)	0,22 ± 0,04	0,49 ± 0,05
$2\beta_3$_D3	(0,05 ± 0,02)	0,08 ± 0,02	0,32 ± 0,02
$2\alpha_4$ _A4	0,27 ± 0,03	0,92 ± 0,04	4,48 ± 0,07
$2\alpha_4$ _C4-D3	(0,07 ± 0,01)	0,11 ± 0,01	4,28 ± 0,05
$3\alpha_1$ _C1	1,09 ± 0,04	1,38 ± 0,03	4,99 ± 0,05
$3\alpha_1$ _C4-D4	1,68 ± 0,04	2,48 ± 0,04	5,55 ± 0,05
$3\alpha_2$ _B1-B2	1,46 ± 0,05	1,86 ± 0,04	5,33 ± 0,06
$3\alpha_2$ _D4	1,61 ± 0,05	1,82 ± 0,04	4,05 ± 0,06
$3\alpha_3$ _A3	1,69 ± 0,06	2,21 ± 0,05	6,33 ± 0,08

Table S7: Aluminum, silicon and sulfur contents measured in luminescent microparticles from samples of the BSM mummy. Values in brackets have an error of over 25%, but the presence of these elements is assured.

S3.4 Other markers: Hg, Pb, As, Sr, Br and Cl

		Concentrations (μg.g^{-1})					
		Hg	**Br**	**Cl**	**Pb**	**Sr**	**As**
Bitumen (DS)	DS(1)	(0,6 ± 0,7)	18.2 ± 1.1	2522 ± 118	<1.3	<0.5	(1.1 ± 0.2)
	DS(2)	<1.8	29. ± 5.9	3140 ± 133	<1.2	<0.8	2.6 ± 0.7
Corpus A (birds)	*1*	<2.8	7.0 ± 1.4	991 ± 36	(2.8 ± 6.0)	15.5 ± 3.1	(1.8 ± 1.5)
	3	(1.0 ± 2.0)	11.0 ± 1.1	1080 ± 40	73.8 ± 6.7	(2.4 ± 1.2)	(3.4 ± 1.3)
	4	<4.3	18.5 ± 1.5	2163 ± 57	(8.8 ± 5.3)	26.9 ± 2.5	<1.2
	6	<2.0	41.0 ± 1.8	8925 ± 152	(1.1 ± 3.0)	21.4 ± 2.3	<1.1
	8	<1.3	8.8 ± 1.1	1200 ± 41	56.5 ± 6.2	(6.8 ± 1.5)	(4.5 ± 1.1)
	10	(2.0 ± 1.9)	11.6 ± 1.3	607 ± 26	(2.8 ± 4.4)	9.9 ± 2.0	(1.4 ± 1.1)
	11	<6.5	35.4 ± 2.0	4662 ± 123	(2.8 ± 4.7)	218.9 ± 6.6	(2.6 ± 1.0)
	12	<3.0	30.9 ± 1.7	10928±138	(2.2 ± 4.8)	18.0 ± 2.2	3.2 ± 1.0
	14	<1.3	10.9 ± 1.1	714 ± 33	70.1 ± 5.6	(2.6 ± 1.0)	<1.2
Corpus B Animals and human	*An1*	<3.9	95.6 ± 4.0	2682 ± 48	1601 ± 33	44.6 ± 5.0	<4.6
	An2(1)	(2.3 ± 2.0)	11.7 ± 1.4	520 ± 38	117.5 ± 8	31.6 ± 3.6	(7.1 ± 1.6)
	An2(2)	<1.4	5.7 ± 0.9	189 ± 16	(5.4 ± 2.2)	21.4 ± 2.9	4.0 ± 0.8
	An3	(0.6 ± 0.7)	11.9 ± 0.6	1915 ± 56	59.7 ± 2.5	7.7 ± 0.8	(3.9 ± 0.6)
	An5	<1.7	10.1 ± 1.1	1757 ± 55	36.7 ± 3.8	(5.2 ± 1.5)	<2.1
	Hum1	(1.0 ± 0.7)	4.7 ± 0.7	218 ± 23	14.8 ± 2.0	8.3 ± 1.3	(0.7 ± 0.5)
	Hum2(1)	(1.2 ± 0.4)	3.0 ± 0.5	332 ± 19	(2.0 ± 1.0)	(3.9 ± 0.9)	(0.4 ± 0.2)
	Hum2(2)	(1.0 ± 1.0)	(3.5 ± 0.9)	191 ± 18	(3.0 ± 2.0)	(5.0 ± 1.8)	<1.0
BSM mummy	$1\alpha_1$	33.7 ± 1.7	82.6 ± 7.6	1876 ± 26	60.8 ± 3.3	25.7 ± 1.1	(2.6 ± 0.6)
	$1\alpha_2$	67.3 ± 12.6	354.2 ± 13.3	1418 ± 13	181 ± 33	125.5 ± 13.5	(8.5 ± 6.2)
	$1\beta_3$	184.8 ± 5.9	207.9 ± 5.0	11441±180	83.0 ± 7.4	37.8 ± 2.5	(9.3 ± 1.5)
	$1\beta_4$	183.5 ± 7.1	254.1 ± 6.3	11381±199	101 ± 9.6	37.0 ± 3.2	11.4 ± 2.0
	$1\beta_5$	186.5 ± 11	214.0 ± 8.2	7547 ± 137	146 ± 20	55.8 ± 6.8	(9.2 ± 1.9)
	$1\beta_6$	184.9 ± 5.4	81.8 ± 3.1	10491±198	51.9 ± 5.4	18.3 ± 1.9	8.9 ± 1.2
	$2\beta_1$	114.3 ± 11	361.6 ± 14.0	7647 ± 99	75.5 ± 25	107.4 ± 13.0	<6.9
	$2\beta_2$	156.0 ± 7.3	262.4 ± 7.1	8693 ± 103	147 ± 13	36.1 ± 4.4	<3.4
	$2\beta_3$	126.6 ± 6.8	296.9 ± 8.2	5530 ± 86	123 ± 14	40.9 ± 4.5	<8.7
	$2\alpha_4$	1691 ± 33	45.1 ± 7.6	4783 ± 117	(13.4 ± 7)	(9.3 ± 4.2)	(3.3 ± 1.4)
	$3\alpha_1$	569.8 ± 9.3	980.4 ± 15.7	1871 ± 5	10.6 ± 2.0	(3.0 ± 1.0)	4.3 ± 0.4
	$3\alpha_2$	2138 ± 66	4100.2 ± 110.3	2599 ± 127	(42 ± 33)	(29.1 ± 13.6)	(9.0 ± 5.9)
	$3\alpha_3$	644.4 ± 10	1091.9 ± 17.1	1472 ± 43	12.6 ± 2.0	(3.0 ± 1.0)	3.3 ± 0.4

Table S8: Mercury, lead, strontium, arsenic and bromine contents measured on homogeneous areas of the Boulogne-sur-Mer mummy and Corpus A and B samples, as well as on Dead Sea bitumen (DS). Values in brackets have an error of over 25%, but the presence of these elements is assured; in several cases, the values could not be measured as they were below the LOD.

S4 LUMINESCENT MINERAL PARTICLES

S4.1 Optical transitions in silicates and carbonates

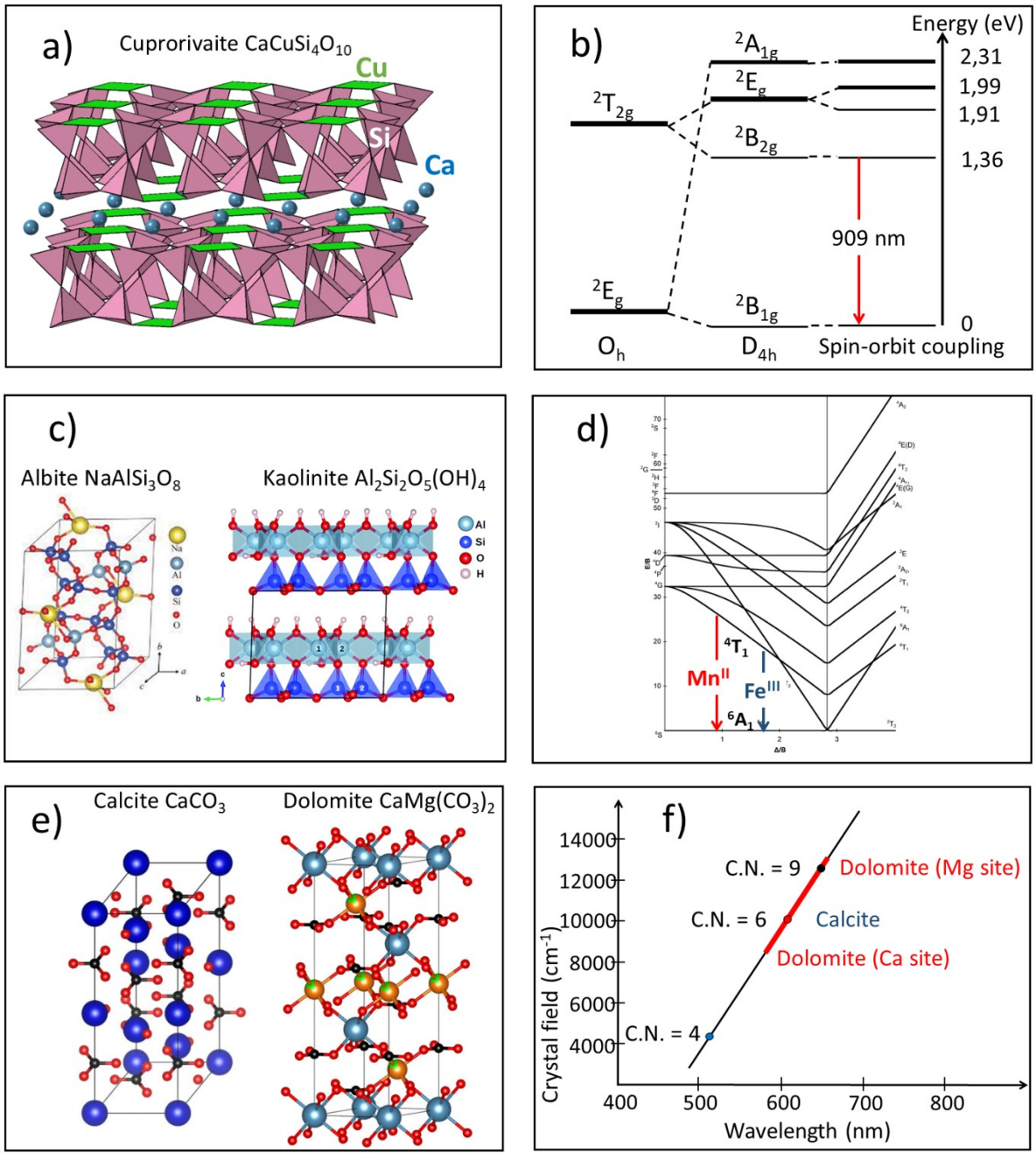

Figure S6: a) Structure of cuprorivaite, the main component of Egyptian blue pigment; b) energy level diagram of Cu^{II} in square planar configuration, showing the $^2B_{2g} \rightarrow {}^2B_{1g}$ transition responsible for the NIR luminescence of Egyptian blue; c) structure of the sodic feldspar albite, and of kaolinite, a clay mineral resulting from the alteration of albite; d) Tanabe-Sugano diagram of d^5 transition metal, showing the transition $^4T_1 \rightarrow {}^6A_1$ responsible for luminescence of Fe^{III} in feldspars, and Mn^{II} in feldspars and carbonates; e) structure of calcite and dolomite; f) variation of the luminescence wavelength of Mn^{II} with the crystal field strength acting on Mn^{II} impurities, as a function of its coordination number (CN).

S4.2 Feldspars and carbonates

The IBIL spectra show several different types of emission bands, which are found in the Boulogne-sur-Mer mummy as well as in other mummies. An interesting example is sample 4, which is a fragment of feather covered with black matter, taken from the mummy of a bird of prey found in Giza (northern Egypt) and dating from the Roman Empire (Fig.S10a), compared with the same type of sample (sample 11) taken from an ibis mummy found in Roda (southern Egypt) and dating from the Late Period (4^{th} century BC) (Fig.S4). Three 1000×1000 μm^2 mappings were carried out on this sample, showing the presence of four different types of spectra. The a-type spectrum (Fig. S10a) is very similar to that observed for the ibis found in Roda (Fig.S4), and shows the presence of feldspar grains (Fe^{III} luminescence) and calcite (Mn^{II} luminescence). These minerals are therefore ubiquitous in northern and southern Egypt. The b-type spectrum (Fig.S10a), found in the second mapping and centered around 650 nm, could be that of a Mg-rich dolomite grain. The third mapping shows two types of spectra (Fig.S10b). The c-type spectrum is a broad luminescence band centered in the blue and extending towards low energies, corresponds to the intrinsic luminescence (atomic defects) often observed in silicates. It is emitted by a large grain (approx. 0.5 mm long), to which is bonded a smaller grain (approx. 0.2 mm) with a complex luminescence spectrum (d-type spectrum). The c-type spectrum is a very broad band covering the entire visible range, probably due to superimposed emission from intrinsic defects and several types of impurity, including Mn^{II} and Fe^{III} in a silicate mineral. The d-spectrum is particularly complex and described in more details in Fig.S10c. It comprises a broad emission Mn^{II} in calcite superimposed with narrow bands due to Ln^{3+} lanthanide ions, of which samarium Sm^{3+} gives the strongest lines. The band at around 900 nm with its underlying structure is unambiguously attributed to neodymium Nd^{3+} ions. Weaker transitions are due to dysprosium Dy^{3+} at trace level. All these attributions are based on the Dieke's diagram shown in Fig.S10d (Wegh et al. 2000). IBIL images 1, 2 and 3 show that Mn^{II} and Ln^{3+} impurities are located in the same grain.

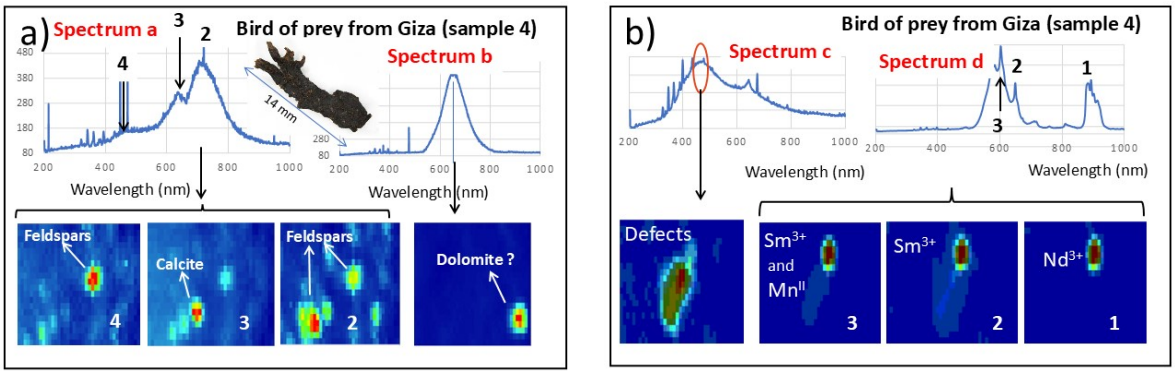

Figure S7: a) IBIL spectra and mappings of three areas (1000×1000 µm^2) of a feather fragment from the mummy of a bird of prey from Giza (sample 4); the IBIL mappings were recorded at selected wavelength ranges (labelled 1 to 4) corresponding to different luminescent peaks; a) a-type spectrum and the corresponding mappings at different wavelength ranges reveal an association of calcite and feldspars particles; this spectrum is very similar with that of sample 11 (Fig. S4); b-type spectrum b and its mapping reveals the possible presence of a dolomite grain; b) the third IBIL mapping reveals the association of two grains stuck together: a silicate grain (about 0.5 mm length) characterized by the emission of intrinsic defects (c-type spectrum), and a calcite grain (about 0.2 mm length) characterized by its Mn^{II} emission and rare earth Nd^{3+}, Sm^{3+} and Dy^{3+} trace elements (d-type spectrum).

S4.3 Copper-based minerals

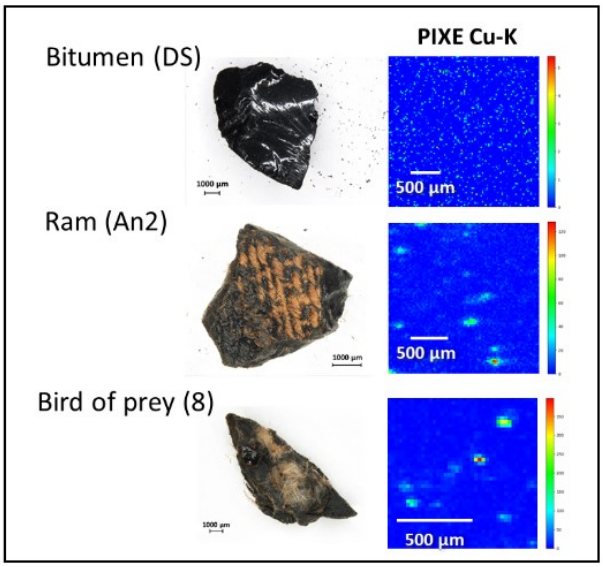

Figure S8: Examples of PIXE mappings of Cu-K_α and K_β emissions in pure bitumen, a ram mummy (An2) and a bird mummy (sample 8). Only mummies show copper-enriched particles.

Some IBIL spectra may deviate from the spectrum expected for pure cuprorivaite (emission centered at 909 nm). Figures 9a-c show grains with a broad, probably composite emission band centered around 920-940 nm. Some Cu-enriched grains are not associated with an IBIL spectrum (Fig.S9d). As these are located in the close vicinity of grains showing luminescence at around 900-940 nm, they are also attributable to cuprorivaite, Also, some of the copper-rich particles that are not luminescent may come from contamination by bronze tools used to prepare

mummies. For example, for the two animal mummies of Fig.S8, the Cu and Sn contents of An2 (a ram mummy) are 76 µg/g and 118±46 µg/g (LOD = 52 µg/g), respectively. The Cu and Sn contents of sample 8 (a bird mummy) are 63 µg/g and 57±39 µg/g (LOD = 24 µg/g), respectively. The Sn content was measured from the Lα line. Although highly imprecise, these Sn contents support the hypothesis of a possible contamination by bronze particles.

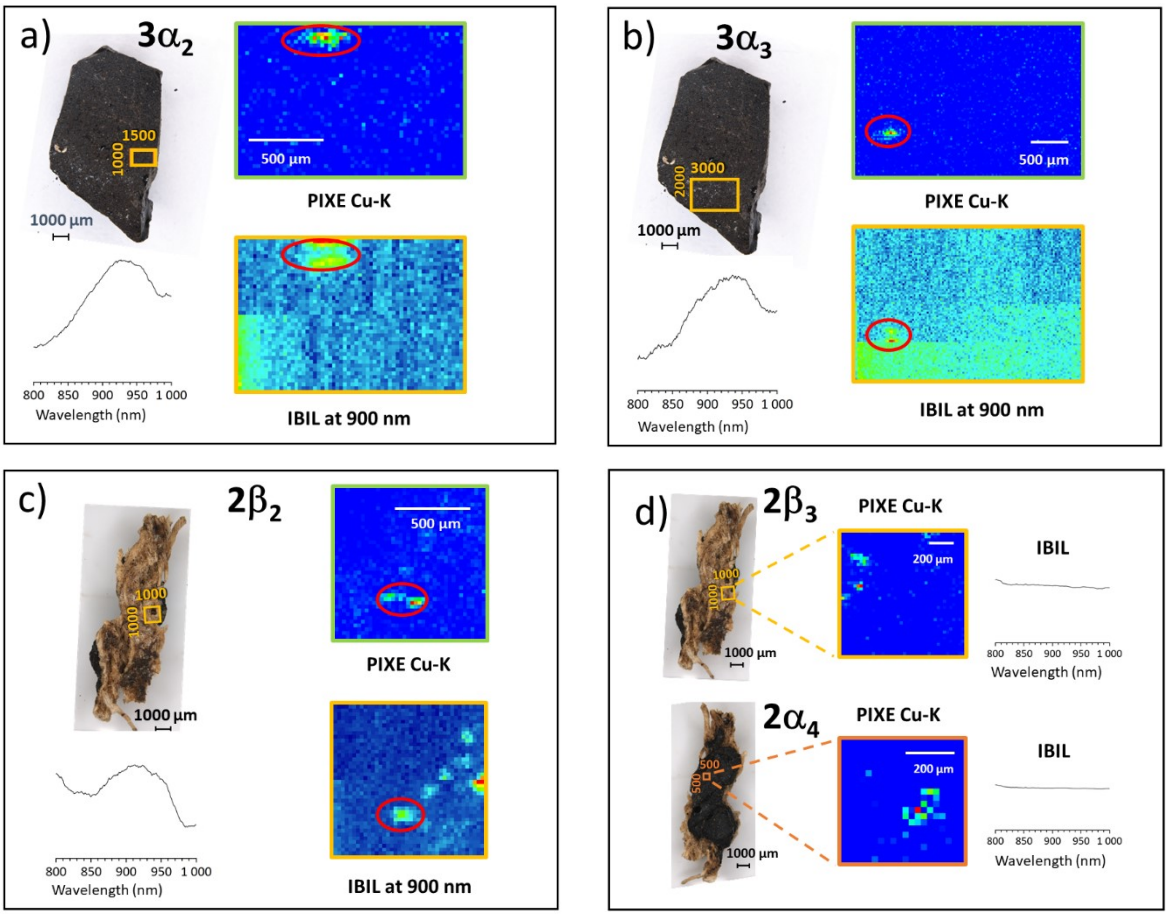

Figure S9: Examples of Cu-K PIXE and NIR-IBIL mappings recorded on the Boulogne-sur-Mer mummy; a) and b) mappings $3\alpha_2$ and $3\alpha_3$; c) mapping $2\beta_2$; d) mappings $2\beta_3$ and $2\alpha_4$ showing Cu-K PIXE spots but no IBIL band.

REFERENCES.

Anduze, O., Gourier, D., Binet, L., Malergue, A., Grossi, V., and Lattuati-Derieux, A. 2025, Identification, quantification and sourcing of fossil hydrocarbon in ancient Egyptian mummies by V and Ni trace elements. *J. Anal. At. Spectrom.* **40**, 487-497. https://doi.org/10.1039/D4JA00442F

Dal-Prà, P. 2004. Rapport de restauration de la momie d'homme du Château-Musée de Boulogne sur Mer. N°6306. C2RMF, Paris.

Dewachter, M. 1979. « Informations relatives à la collection du Comte de Saint-Ferriol et fournies par son journal de voyage ». In *Kueny, G.; Yoyotte, J. Grenoble, musée des Beaux-Arts : Collection égyptienne*, 53. Paris: Editions de la Réunion des Musées Nationaux.

Pichon, L., Beck, L., Walter, Ph., Moignard, B., etand Guillou. T. 2010. A New Mapping Acquisition and Processing System for Simultaneous PIXE-RBS Analysis with External Beam. *Nucl. Instrum. Methods B* **268**, 2028-2033. https://doi.org/10.1016/j.nimb.2010.02.124

Pichon, L., Calligaro, T., Gonzalez, V., Lemasson, Q., Moignard, B., and Pacheco, C. 2015, Programs for visualization, handling and quantification of PIXE maps at the AGLAE facility. *Nucl. Instrum. Methods B* **363**, 48-54. https://doi.org/10.1016/j.nimb.2015.01.086

Wegh, R.T., Meijerink, A., Lamminmäki, R.J., and Hölsä, J. 2000, Extending Dieke's diagram, *J. Lumin*. **87-89**, 1002-1004. https://doi.org/10.1016/S0022-2313(99)00506-2

Ziegler, J.F., Ziegler, M.D., and Biersack, J.P. 2010, SRIM-The stopping and range of ions in matter (2010). *Nucl. Instrum. Methods B* **268**, 1818-1823. https://doi.org/10.1016/j.nimb.2010.02.091